



## Parasitic Capacitance Modeling of Copper-Foiled Medium-Voltage Filter Inductors Considering Fringe Electrical Field

Zhao, Hongbo; Huang, Zhizhao; Dalal, Dipen Narendra; Jørgensen, Jannick Kjær; Jørgensen, Asger Bjørn; Wang, Xiongfei; Munk-Nielsen, Stig

*Published in:*  
IEEE Transactions on Power Electronics

*DOI (link to publication from Publisher):*  
[10.1109/TPEL.2020.3048226](https://doi.org/10.1109/TPEL.2020.3048226)

*Publication date:*  
2021

*Document Version*  
Accepted author manuscript, peer reviewed version

[Link to publication from Aalborg University](#)

*Citation for published version (APA):*  
Zhao, H., Huang, Z., Dalal, D. N., Jørgensen, J. K., Jørgensen, A. B., Wang, X., & Munk-Nielsen, S. (2021). Parasitic Capacitance Modeling of Copper-Foiled Medium-Voltage Filter Inductors Considering Fringe Electrical Field. *IEEE Transactions on Power Electronics*, 36(7), 8181-8192. Article 9311400. <https://doi.org/10.1109/TPEL.2020.3048226>

### General rights

Copyright and moral rights for the publications made accessible in the public portal are retained by the authors and/or other copyright owners and it is a condition of accessing publications that users recognise and abide by the legal requirements associated with these rights.

- Users may download and print one copy of any publication from the public portal for the purpose of private study or research.
- You may not further distribute the material or use it for any profit-making activity or commercial gain
- You may freely distribute the URL identifying the publication in the public portal -

### Take down policy

If you believe that this document breaches copyright please contact us at [vbn@aub.aau.dk](mailto:vbn@aub.aau.dk) providing details, and we will remove access to the work immediately and investigate your claim.



# Parasitic Capacitance Modeling of Copper-Foiled Medium-Voltage Filter Inductors Considering Fringe Electrical Field

Hongbo Zhao, *Student Member, IEEE*, Zhizhao Huang, Dipen Narendra Dalal, *Student Member, IEEE*, Jannick Kjær Jørgensen, Asger Bjørn Jørgensen, Xiongfei Wang, *Senior Member, IEEE*, and Stig Munk-Nielsen, *Member, IEEE*,

**Abstract-** This paper characterizes three parasitic capacitances in copper-foiled medium-voltage inductors. It is found that the conventional modeling method overlooks the effect of the fringe field, which leads to inaccurate modeling of parasitic capacitances in copper-foiled inductors. To address this problem, the parasitic capacitances contributed by the fringe electrical field is identified first, and a physics-based analytical modeling method for the parasitic capacitances contributed by the fringe electrical field is proposed, which avoids using any empirical equations. The total parasitic capacitances are then derived for three different cases with three different core potentials, from which a three-terminal equivalent circuit is derived, and thus, the parasitic capacitances in copper-foiled inductors are explicitly identified. The calculated results show a close agreement with the measured capacitance by using an impedance analyzer. Two recommendations for reducing the parasitic capacitances in copper-foiled inductors are given in this paper.

**Index terms-** Parasitic capacitance, copper-foiled, medium-voltage, filter inductor, fringe field, physics-based modeling.

## I. INTRODUCTION

Thanks to the advances in the power semiconductor devices, the wide-band-gap (WBG) transistors are widely used in modern power conversion systems [1], where the power converters can be designed with higher switching frequency and less switching losses [2], [3]. Yet, the high dv/dt problem becomes more significant during the switching transitions of WBG transistors [4]. Under the high dv/dt conditions, the parasitic capacitances of passive and active power components, such as the common-mode capacitance of gate drivers [5], [6], the ground capacitance of heatsink [7], the parasitic capacitance in power modules [8], [9], and the parasitic capacitance in transformers [10-12] and inductors [13-15], can bring large common-/differential-mode current into the converter circuit [13], causing electromagnetic interferences [4] and accelerating the aging of power components [16]. It is also reported that the parasitic capacitances in medium voltage (MV) inductors are larger

than them in low voltage inductors due to the required higher inductance and extra insulation [13].

The windings of inductors are commonly constructed with round cables for a low cost. Yet, in high-frequency applications, both the copper foil and the litz wire are commonly used for a lower ac-resistance [17], and the copper-foil is more popular in high-voltage and high-power applications [17-20], due to its higher power density and more flexibility than round cables and Litz wires in the manufacturing process. However, the intra-winding capacitance of the copper-foiled inductors and transformers is large due to the extensive interleaving of the windings [17], which is not desirable in applications with high dv/dt operations. Therefore, it is important to characterize and reduce the parasitic capacitances in copper-foiled filter inductors, especially when they are used in the converters based on WBG devices.

A few works have been reported on modeling the parasitic capacitance of copper-foiled magnetic components [17], [20], [21]. Basically, the parasitic capacitance in magnetic devices is divided into static capacitance and dynamical capacitance.

- 1) Static capacitance [21], [22]. It represents the capacitance between two planes when disconnected, where there is no ohmic voltage drop on each plane. Therefore, the static capacitance is merely dependent on the geometrical structure and material information of the two planes.
- 2) Dynamical capacitance [21], [22]. This capacitance represents the total electrical field energy stored between any two planes, which is related to the voltage potential distribution. In practice, the voltage potential on each plane is not a constant value, due to the current flows through the winding, which results in ohmic voltage drops in the windings. The dynamical capacitance can be calculated by the static capacitance and dynamical voltage potential distribution.

In [17], the parasitic capacitance of a copper-foil-based transformer between the primary side and secondary side is calculated by using the formula of parallel plate capacitance, which is, however, merely a static capacitance, and thus fails to capture the dynamical capacitance in practice [14], [21], [22]. An air-coiled inductor wound by copper foils is modeled in [20], where the first resonant frequency caused by the intra-winding capacitance is identified, yet the modeling of parasitic

This work is supported by MVolt project, which is co-funded by the Department of Energy Technology of Aalborg University, Innovation Fund Denmark, Siemens Gamesa, Vestas Wind System, and KK wind solutions (*Corresponding author: Zhizhao Huang and Xiongfei Wang*)

H. Zhao, D. Dalal, J. Jørgensen, A. Jørgensen, X. Wang, and S. Munk-Nielsen, are with the Department of Energy Technology, Aalborg University, Aalborg, Denmark (e-mail: [hzh@et.aau.dk](mailto:hzh@et.aau.dk))

Z. Huang is with the School of Electrical and Electronic Engineering, Huazhong University of Science and Technology, Wuhan, China.

capacitance is not addressed. In [21], both the static and dynamical capacitances are calculated, considering the eddy current effects. However, the core is assumed to be always floating in this work, where only one equivalent capacitance can be calculated. An improved modeling method is reported in [22] to consider the grounding effects of the magnetic core, yet it is only focused on the round-cable based inductors. As found later in this paper, the method reported in [22] fails to characterize the capacitive couplings between the core and terminals of the copper-foiled inductor, where the fringe field between the winding and core is significant for modeling the parasitic capacitance in typical copper-foiled inductors.

In [23], a modeling method is proposed to calculate the parasitic capacitance of a high-power transformer, where the fringe electrical field between different sections are considered by using the empirical equations that are derived from very-large-system-integration (VLSI) applications [24]. The parasitic capacitance contributed by the fringe field is usually neglected in most previous modeling methods [10, 12, 14, 20, 25]. The parasitic capacitance introduced by the fringe field has also been discussed in transmission lines [26], antenna applications [27], and micro electronics [28]. However, these empirical equations are actually restricted by the geometrical structure [24], which is not applicable to model the fringe-field capacitance between the winding and core in copper-foiled inductors due to a more complex geometrical structure.

This article thus attempts to fill this gap by first identifying the fringe electrical field in the copper-foiled medium-voltage (MV) filter inductors, based on which, a physics-based modeling method for static and dynamical capacitances is then proposed. Subsequently, the total capacitance of the filter inductors is obtained by summing the dynamical capacitance contributed by the fringe field, the electrical field between the inner layer and core, the electrical field between windings, and the electrical field between two adjacent layers. The theoretical calculations show good agreement with the measurements of a practical copper-foiled inductor by using an impedance analyzer.

## II. MV COPPER-FOILED INDUCTORS

An MV copper-foiled inductor (30 mH) is taken as an example in this study. The MV inductor is designed for a 5kHz 2-level voltage source converter based on SiC MOSFETs with 4.16 kV line-to-line ac voltage and 6 kV dc-link voltage. The insulation level of this inductor is 10 kV, and the current rating is 8 A (rms). The windings and insulation of the inductor are constructed by copper- and mylar-foils, which are arranged in multiple layers. Two U-type amorphous cores are used for the magnetic loop with an air gap in between.

The schematics of the studied MV copper-foiled inductor are given in Fig. 1. Fig. 1 (a) shows the front view and Fig. 1(b) gives the cross-section view. Two windings are connected in parallel for sharing the current. Spacers are used to reduce the capacitive couplings between the inner layer and core, and they will be modeled later.

The parameters of the studied MV foil-based inductor are summarized in Table I, along with the definitions of symbols used in Fig. 1.

The insulation material is selected as Dupont Mylar A [29]. The material of the bobbin and spacer is Durethan BKV 30 H3 [30], which is based on Polyamide 6 with 30% glass-reinforced. The values for the relative permittivity of materials are listed in Table II, which are identified from the datasheet. The conductivity of the amorphous core is  $130 \mu\Omega/\text{cm}$ , according to the datasheet [32].

The insulation material is selected as Dupont Mylar A [29]. The material of the bobbin and spacer is Durethan BKV 30 H3 [30], which is based on Polyamide 6 with 30% glass-reinforced. The values for the relative permittivity of materials are listed in Table II, which are identified from the datasheet.

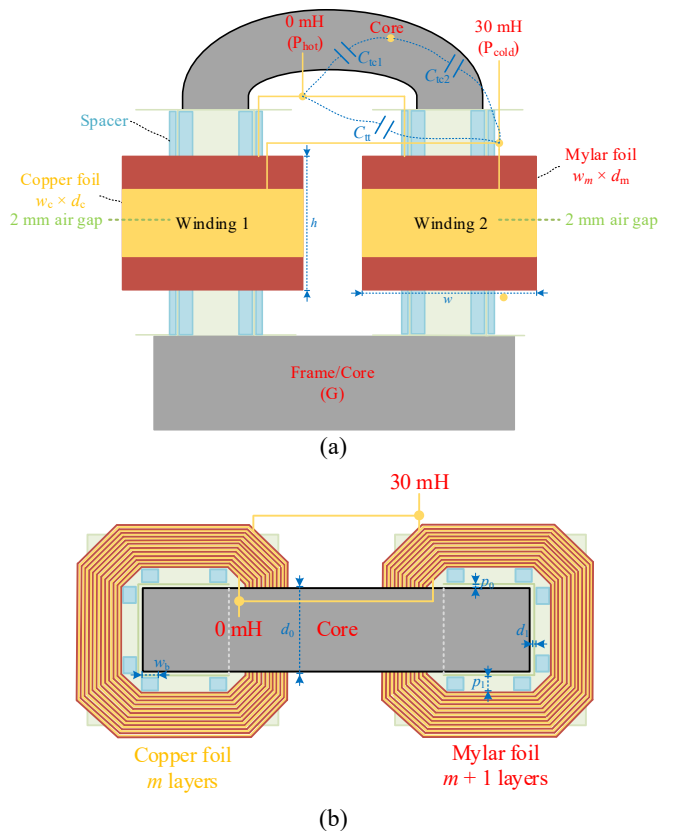


Fig. 1. Schematics of the studied MV copper-foiled inductor. (a) Front view. (b) Cross-sectional view schematic of an MV copper-foiled inductor.

Table I. Key parameters of the MV foil-based inductor

Description	Symbol	Value
Thickness of the copper foil	$d_c$	0.05 mm
Width of the copper foil	$w_c$	30 mm
Thickness of the mylar foil	$d_m$	0.05 mm
Width of the mylar foil (Height of the winding)	$w_m$ ( $h$ )	60 mm
Distance between the two windings	$p_w$	19 mm
Width of the winding	$w$	55.5 mm
Width of the spacer	$w_b$	10 mm

Thickness of the core	$d_0$	40 mm
Distance of the air gap between the bobbin and core	$p_0$	1.5 mm
Distance between the inner layer and bobbin	$p_1$	12 mm
Thickness of the bobbin	$d_1$	2 mm
Number of layers	$m$	190
Total inductance (designed value)	$L$	30 mH

TABLE II. RELATIVE PERMITTIVITY OF THE MATERIAL

Description	Symbol	Value
Relative permittivity of the mylar foil [29]	$\epsilon_m$	3.25
Relative permittivity of the bobbins and spacers [30]	$\epsilon_b$	4.0
The permittivity of vacuum [31]	$\epsilon_0$	$8.82 \times 10^{-12}$ F/m

In Fig. 1, the terminal labeled as “0 mH” is also defined as the hot terminal  $P_{hot}$ , which locates at the inner layer. The terminal labeled as “30 mH” is defined as the cold terminal  $P_{cold}$ , which locates at the outer layer. The core/frame is also labeled as G.

The focus of this paper is to analytically model the equivalent capacitance between  $P_{hot}$  and  $P_{cold}$   $C_{it}$ , between  $P_{hot}$  and G  $C_{ic1}$ , and between  $P_{cold}$  and G  $C_{ic2}$ , based on the geometrical and material information of the copper-foiled inductors.

### III. MODELING OF THE FRINGE FIELD CAPACITANCE

In this section, the electrical field in the copper-foiled inductors are identified. Based on [22], most capacitive couplings in copper-foiled inductors are identified, which includes the couplings between the inner layer and core, between two different layers, and between two windings. Due to the special structure of copper-foiled inductor, there is only one turn in a single layer. Therefore, the couplings between turns are the same as those between layers.

However, the fringe field between winding and core is not considered in the modeling in [22], which will be proved that is not neglectable in copper-foiled inductors by the later sections of this paper.

#### A. Identify the fringe electrical field

A finite element method (FEM) simulation is given to identify the fringe field in the copper-foiled inductors by using Ansys, which is presented in Fig. 2. In the simulation, the voltage potential along the layers of the copper-foils is configured equally, therefore, the electrical field strength between two adjacent layers is zero in this simulation. The core is configured as reference ground. 19-layer copper-foil and 20-layer mylar-foil are used to construct the winding. In this simulation, the thickness of the copper- and mylar-foil is configured as 0.5mm, where the distance between the inner-layer and core is 4 mm. The width of the copper-foil is 30 mm, where the width of the mylar-foil is 60 mm in Fig. 2. The parameters of material used in FEM simulation are the same as Table II.

It is worth mentioning that the geometrical parameters of the copper-foiled inductor in FEM simulations are not exactly the same as the designed value since the main target here is to identify the all possible electrical field existed around the copper-foiled inductor.

According to Fig. 2, although the electrical field is strongest between the inner-layer and core, the fringe field between the winding and core are still obvious on both edges. Both the fringe field between the sidewall of the inductor and core, and the fringe field between the top-surface and core can be identified from Fig. 2.

The energy stored in the fringe electrical field will contribute to an equivalent capacitance (The fringe field mentioned in this paper is the fringe electrical field). This capacitance cannot be neglected in the copper-foiled inductors since the extensive area of the sidewall and top surface of the copper-foiled inductors. Usually, the fringe field is neglected for modeling the parasitic capacitance of inductors in previous research since its impacts are limited. However, in the copper-foiled inductor, due to a large number of layers, the sidewall area of the copper-foils is significant. Therefore, the impacts of the fringe field may not be neglected for the purpose of modeling the parasitic capacitances.

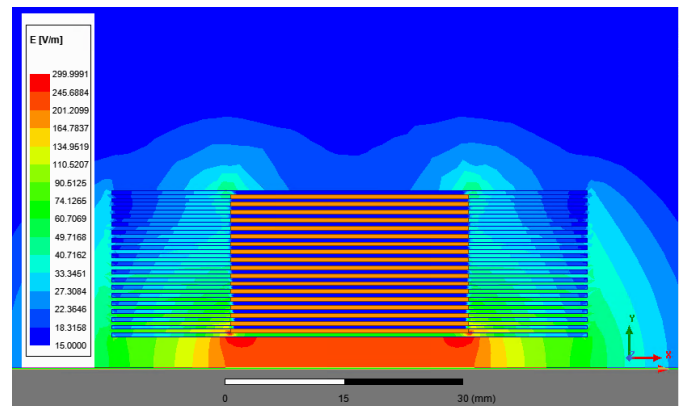


Fig. 2 Fringe field between the winding and core of the copper-foil inductors

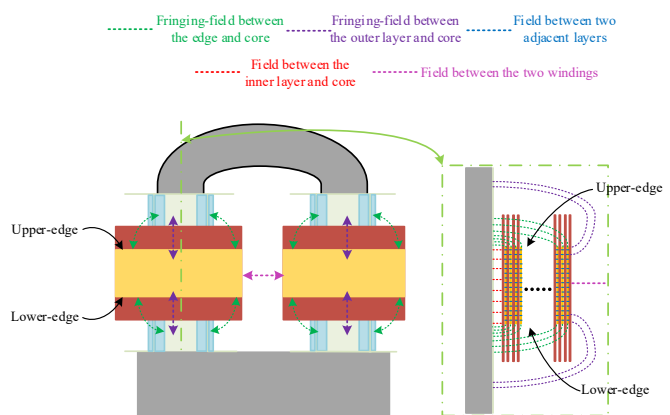


Fig. 3 Identify the capacitive couplings in copper-foiled MV inductors

Fig. 3 illustrates the field distributions between the winding and core of the copper-foiled inductor. Besides the well-known field between two neighbour layers (illustrated with blue lines), the field between the inner layer and core

(illustrated with red lines), and field between the two windings (illustrated with pink lines), it also contains the fringe field between the sidewall of winding and core (illustrated with green lines) and the fringe field between the top-surface and core (illustrated with purple lines).

### B. Empirical equation in VLSI applications

In VLSI applications [24], a schematic to illustrate the parasitic capacitance with considering the fringe field effect is presented in Fig. 4.

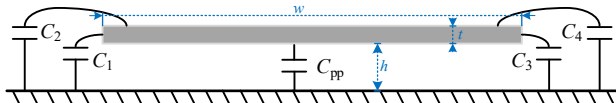


Fig. 4 Schematic of a chip and ground in VLSI applications

In Fig. 4,  $C_1$ ,  $C_2$ ,  $C_3$ , and  $C_4$  are the parasitic capacitance contributed by the fringe field.  $C_{pp}$  is the parallel capacitance between the bottom surface and reference ground. An empirical equation [25], which is widely used in VLSI applications, is given to calculate the total parasitic capacitance.

$$C_{\text{total}} = C_1 + C_2 + C_3 + C_4 + C_{pp} \approx \epsilon_0 \epsilon_r \times \left( \frac{w}{h} + 0.77 + 1.06 \times \left( \frac{w}{h} \right)^{0.25} + 1.06 \times \left( \frac{t}{h} \right)^{0.5} \right) \quad (1)$$

However, there are some restrictions for applying the empirical equation in calculating the parasitic capacitance of copper-foiled inductors:

- 1) Only applicable for the cases with simple structures. In VLSI applications, the structure of the conductor is with only one layer. The conductor is assumed to be surrounded by the same material, therefore, only one relative permittivity is used in (1).
- 2) Only applicable for the cases with specific geometrical structures. The empirical equation requires  $w/h > 0.3$  and  $t/h < 10$ . Otherwise, it can introduce significant errors.
- 3) The calculated capacitance by the empirical equation is the static capacitance, where the voltage potential on the inductor is assumed to be the same.

For the copper-foiled inductor illustrated in Fig. 1, it has a more complex geometrical structure than the structure in Fig. 4. Besides, the voltage potential is distributed linear on the windings in practice, where the calculated static capacitance from the empirical equation cannot be correctly revealed the energy stored in the electrical field, which is typically represented by the dynamical capacitances.

### C. Physics-based modeling method of the fringe field capacitance

The parasitic capacitance contributed by the fringe field is modeled as two independent capacitances, which are, the fringe field capacitance between the sidewall and core of the inductor, and the fringe field capacitance between the top-surface and core. The static capacitances are derived first. The

dynamical capacitance will be modeled based on the derived static capacitance.

Some assumptions are made before modeling the fringe field capacitance:

- 1) The electrical lines between the sidewall of winding and core are assumed to be an arc of a 90-degree sector, which is illustrated in Fig. 5(a), where the electrical field is orthogonal to the conductor surfaces.
- 2) The electrical lines between the top-surface and core of the inductor are the arc of a half-circle plus a straight line, which is also illustrated in Fig. 5(b). The electrical field is orthogonal to the conductor surfaces. This is an approximation for describing the field line between the top-surface and core of the inductor shown in Fig. 5.
- 3) The voltage potential on the sidewall of winding is continuous. The sidewall of the mylar-foil is assumed to have a virtual voltage potential, which is contributed by the fringe field from the top and bottom surface of each copper-foil approximately. However, it is only applicable for the cases that  $w_c \gg d_c$ , which is not strict for normal copper-foils. A schematic to illustrate the assumption is presented in Fig. 6.
- 4) The core is a perfect conductor. The voltage potential on the core is always the same.
- 5) The voltage potential on the same layer is assumed to be the same. The error introduced by this assumption can become less when the number of layers is larger.

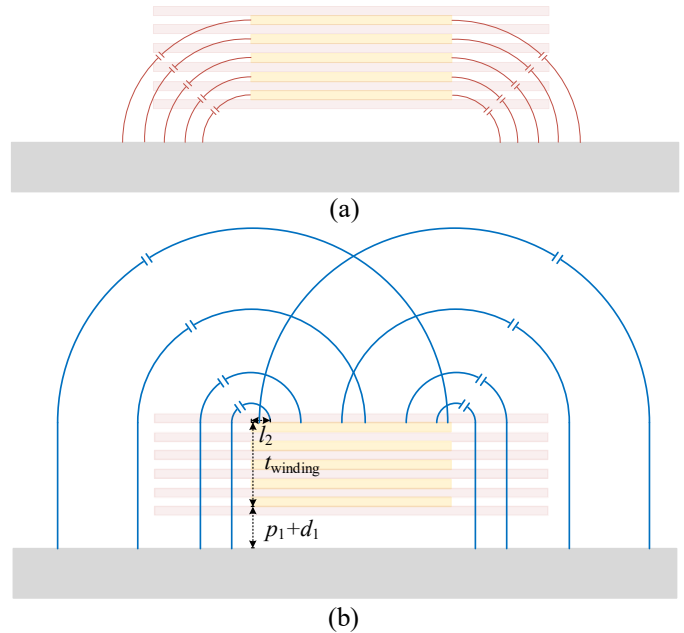


Fig. 5 Elementary capacitances contributed by the fringe field. (a) elementary capacitance between the sidewall and core; (b) elementary capacitance between the top-surface and core.

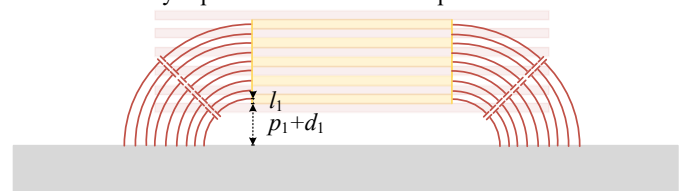


Fig. 6 Approximation made for distributing the voltage potential continuously on the sidewall

### C.1. Static capacitance

In order to calculate the static capacitance contributed by the fringe field, all copper-foils are assigned to have the same voltage potential. The capacitance contributed by the fringe field is classified into two parts, which are the capacitance between the sidewall of winding and core, and between the top-surface and core, respectively.

#### C.1.1 Static capacitance between the sidewall of winding and core

The elementary static capacitance contributed by the fringe field between the sidewall of winding and core is derived in (2) according to Fig. 6.

$$C_{\text{ele\_sc}} = \frac{2\varepsilon_{d1}\varepsilon_0 dl_1}{\pi(l_1 + p_1 + d_1)} \quad (2)$$

$l_1$  is the direct distance between the elementary capacitance and the start point at the sidewall.  $\varepsilon_{d1}$  is the dynamical relative permittivity, which is contributed by both air and mylar-foils. At different layers, the contributed ratio on the equivalent permittivity of the mylar foil and air are different due to the different geometrical structures. Therefore,  $\varepsilon_{d1}$  should be related to the position of the elementary capacitance, which can be approximately presented as (3).

$$\varepsilon_{d1} \approx \frac{p_1 + d_1 + \frac{1 + \varepsilon_c}{2} l_1}{l_1 + p_1 + d_1} \quad (3)$$

The equivalent static capacitance between the two sidewalls of winding and core for single winding in 2-dimension is presented in (4).

$$\begin{aligned} C_{2d\_sc} &= 2 \int_0^{t_{\text{winding}}} C_{\text{ele\_sc}} \\ &= 2 \int_0^{t_{\text{winding}}} \frac{2\varepsilon_{d1}\varepsilon_0}{\pi(l_1 + p_1 + d_1)} dl_1 \end{aligned} \quad (4)$$

A coefficient two is used in (4) since there are two sidewalls in each winding.

#### C.1.2 Static capacitance between the top-surface of winding and core

Similarly, the elementary static capacitance contributed by the fringe field between the top-surface of winding and core is derived in (5) according to Fig. 5.

$$C_{\text{ele\_tc}} = \frac{\varepsilon_{d2}\varepsilon_0 dl_2}{\pi l_2 + p_1 + d_1 + t_{\text{winding}}} \quad (5)$$

$l_2$  is the direct distance between the elementary capacitance and the start point at the top surface.  $\varepsilon_{d2}$  is the dynamical relative permittivity, which can be presented as (6).

$$\begin{cases} \varepsilon_{d2} = \frac{p_1 + d_1 + \frac{1 + \varepsilon_c}{2} t_{\text{winding}} + \pi l_2}{p_1 + d_1 + t_{\text{winding}} + \pi l_2} & (l_2 < \frac{w_m - w_c}{2}) \\ \varepsilon_{d2} = 1 & (l_2 \geq \frac{w_m - w_c}{2}) \end{cases} \quad (6)$$

The equivalent static capacitance between the top surface of winding and core in 2-dimension is presented in (7).

$$\begin{aligned} C_{2d\_tc} &= 2 \int_0^{w_{\text{foil}}} C_{\text{ele\_tc}} \\ &= 2 \int_0^{w_{\text{foil}}} \frac{\varepsilon_{d2}\varepsilon_0}{\pi l_2 + p_1 + d_1 + t_{\text{winding}}} dl_2 \end{aligned} \quad (7)$$

Due to the same voltage potential on all copper-foils, there is no parasitic capacitance between adjacent layers. The equivalent parasitic capacitance between the inner layer and core is derived as (8).

$$\begin{cases} C_{2d\_lc} = \frac{\varepsilon_{s1}\varepsilon_0 w_{\text{foil}}}{d_m + p_1 + d_1} \\ \varepsilon_{s1} = \frac{d_1 \varepsilon_b + p_1 + d_m \varepsilon_m}{d_m + p_1 + d} \end{cases} \quad (8)$$

Then, the total 2D equivalent capacitance illustrated in Fig. 4 is presented as (9).

$$C_{2d\_total} = C_{2d\_sc} + C_{2d\_tc} + C_{2d\_lc} \quad (9)$$

By substituting the geometrical and material parameters used given at the beginning of Section III-A, a comparison of parasitic capacitance obtained using the FEM simulation, the empirical equations and the proposed modeling method versus the number of copper-foil layers is given in Fig. 7, where the proposed model shows a better agreement with FEM simulations than using the empirical equation (1).

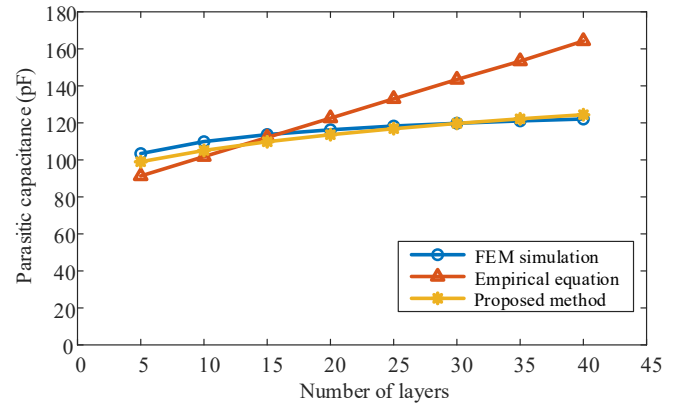


Fig. 7 Comparison of the static capacitances obtained using the FEM simulation, the empirical equations, and the proposed modeling method [24], respectively.

### C.2. Dynamical capacitance

The dynamical capacitance is dependent on both static capacitance and practical voltage potential disturbance. Three cases with different voltage potential distributions are considered in this paper. The dynamical capacitance between the sidewall of winding and core, between the top-surface and core are calculated, respectively.

In Fig. 8, the voltage potential on the inner layer is assumed to be 0, where the voltage potential on the outer layer is assumed to be  $V_1$ .

Case 1: Core is floating. The schematic of Case 1 is illustrated in Fig. 8(a). [14] indicates that the core potential is

floated around  $(0+V_1)/4$  in inductors with multiple layer structures. 0 and  $V_1$  are the voltage potential at the terminals of the inductor.

Case 2: Core is connected to the hot layer, where the core potential is equal to 0. The schematic of Case 2 is illustrated in Fig. 8(b).

Case 3: Core is connected to the cold layer, where the core potential is equal to  $V_1$ . The schematic of Case 3 is illustrated in Fig. 8(c).

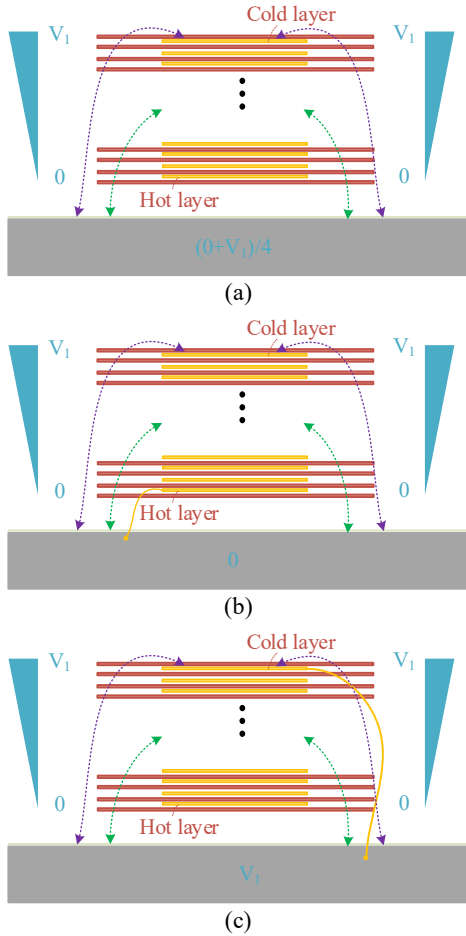


Fig. 8 Schematic of the winding with linear voltage potential distribution. a) Case 1: Core is floating; b) Case 2: Core is connected to the hot layer; c) Case 3: Core is connected to the cold layer.

In the three cases, the voltage potential on the copper-foils is distributed linearly. Therefore, the voltage potential is not equal at different layers of foil-winding. The energy-conservation law is used to derive the dynamical capacitance in this section.

### C.2.1 Dynamical capacitance between the sidewall of winding and core

In Case 1, the elementary energy stored between the sidewall of the winding and core is presented as (10).

$$\begin{aligned} dW_{sc\_case1} &= \frac{1}{2} C_{ele\_sc} \left[ \left( 0 - \frac{0+V_1}{4} \right) + (V_1 - 0) \frac{l_1}{t_{winding}} \right]^2 \\ &= \frac{1}{2} \frac{2\varepsilon_{d1}\varepsilon_0}{\pi(l_1 + p_1 + d_1)} \left[ \left( 0 - \frac{0+V_1}{4} \right) + (V_1 - 0) \frac{l_1}{t_{winding}} \right]^2 dl_1 \end{aligned} \quad (10)$$

where the total energy is given as

$$\begin{aligned} W_{sc\_case1} &= 2 \iint_{A1} dW_{sc\_case1} \\ &= 2 \iint_{A1} \frac{1}{2} \frac{2\varepsilon_{d1}\varepsilon_0}{\pi(l_1 + p_1 + d_1)} \left[ \left( 0 - \frac{0+V_1}{4} \right) + (V_1 - 0) \frac{l_1}{t_{winding}} \right]^2 dl_1 \end{aligned} \quad (11)$$

$A1$  is the surface of the sidewall of the winding in 3-dimensional. Since there are two sidewalls in a single winding, there is a coefficient 2 in front of the integration.

Then, the equivalent sidewall-to-core capacitance to represent the stored energy is derived by

$$\begin{aligned} W_{sc\_case1} &= \frac{1}{2} C_{eq\_sc\_case1} (V_2 - V_1)^2 \\ C_{eq\_sc\_case1} &= \frac{2W_{sc\_case1}}{(V_2 - V_1)^2} \end{aligned} \quad (12)$$

Similarly, the equivalent sidewall-to-core capacitance in Case 2 and Case 3 is presented as (13) and (14), respectively.

$$\begin{cases} W_{sc\_case2} = 2 \iint_{A1} \frac{1}{2} \frac{2\varepsilon_{d1}\varepsilon_0}{\pi(l_1 + p_1 + d_1)} \left[ 0 + (V_1 - 0) \frac{l_1}{t_{winding}} \right]^2 dl_1 \\ C_{eq\_sc\_case2} = \frac{2W_{sc\_case2}}{(V_1 - 0)^2} \end{cases} \quad (13)$$

$$\begin{cases} W_{sc\_case3} = 2 \iint_{A1} \frac{1}{2} \frac{2\varepsilon_{d1}\varepsilon_0}{\pi(l_1 + p_1 + d_1)} \left[ (0 - V_1) + (V_1 - 0) \frac{l_1}{t_{winding}} \right]^2 dl_1 \\ C_{eq\_sc\_case3} = \frac{2W_{sc\_case3}}{(V_1 - 0)^2} \end{cases} \quad (14)$$

### C.2.2 Dynamical capacitance between the top-surface of winding and core

In Case 1, the elementary energy stored between the top surface and core is presented as (14).

$$\begin{aligned} dW_{tc\_case1} &= \frac{1}{2} C_{ele\_tc} \left[ \left( V_1 - \frac{0+V_1}{4} \right) + (V_1 - V_1) \frac{l_2}{t_{winding}} \right]^2 \\ &= \frac{1}{2} \frac{\varepsilon_{d2}\varepsilon_0}{\pi l_2 + p_1 + d_1 + t_{winding}} \left[ \left( V_1 - \frac{0+V_1}{4} \right) + (V_1 - V_1) \frac{l_2}{t_{winding}} \right]^2 dl_2 \end{aligned} \quad (15)$$

If the boundary surface of the top layer in the winding is defined as  $A2$  in 3-dimensional, the equivalent top-surface to core capacitance in Case 1 is obtained as

$$\begin{cases} W_{tc\_case1} = 2 \iint_{A2} \frac{1}{2\pi l_2 + p_1 + d_1 + t_{winding}} \frac{\epsilon_{d2} \epsilon_0}{\left[ \left( V_1 - \frac{0+V_1}{4} \right) + (V_1 - V_1) \frac{l_2}{t_{winding}} \right]^2} dl_2 \\ C_{eq\_tc\_case1} = \frac{2W_{tc\_case1}}{(V_1 - 0)^2} \end{cases} \quad (16)$$

Similarly, the equivalent top-surface to core capacitance in Case 2 and Case 3 is calculated as (17) and (18), respectively.

$$\begin{cases} W_{tc\_case2} = 2 \iint_{A2} \frac{1}{2\pi l_2 + p_1 + d_1 + t_{winding}} \frac{\epsilon_{d2} \epsilon_0}{\left[ (V_1 - 0) + (V_1 - V_1) \frac{l_2}{t_{winding}} \right]^2} dl_2 \\ C_{eq\_tc\_case2} = \frac{2W_{tc\_case2}}{(V_1 - 0)^2} \end{cases} \quad (17)$$

$$\begin{cases} W_{tc\_case3} = 2 \iint_{A2} \frac{1}{2\pi l_2 + p_1 + d_1 + t_{winding}} \frac{\epsilon_{d2} \epsilon_0}{\left[ (V_1 - V_1) + (V_1 - V_1) \frac{l_2}{t_{winding}} \right]^2} dl_2 \\ C_{eq\_tc\_case3} = \frac{2W_{tc\_case3}}{(V_1 - 0)^2} \end{cases} \quad (18)$$

### C.2.3 Dynamical capacitance in total

To sum  $C_{eqsc}$  and  $C_{eqtc}$  in the three cases, the dynamical parasitic capacitance  $C_{eq\_fringe}$  contributed by the fringe field in the single winding is presented in (19).

$$\begin{aligned} C_{eqfringe\_case1} &= C_{eq\_sc\_case1} + C_{eq\_tc\_case1} \\ C_{eqfringe\_case2} &= C_{eq\_sc\_case2} + C_{eq\_tc\_case2} \\ C_{eqfringe\_case3} &= C_{eq\_sc\_case3} + C_{eq\_tc\_case3} \end{aligned} \quad (19)$$

## IV. TOTAL CAPACITANCE

Besides the fringe field capacitance, the inner layer to core capacitance, layer to layer capacitance, and winding-to-winding capacitance need to be considered in order to obtain the total capacitance of the copper-foiled inductor, where the basic principle has been introduced in [22]. However, the equations of the copper-foiled inductor are not exactly the same due to the different geometrical structures.

The equivalent inner layer to core capacitance  $C_{eqlc}$  is calculated for Case 1, Case 2, and Case 3, respectively.

$$\begin{aligned} C_{eqlc\_case1} &= \left( \frac{1}{16} - \frac{1}{4m} + \frac{1}{3m^2} \right) \iint_{A3} C_{ele\_lc} \\ C_{eqlc\_case2} &= \frac{1}{3m^2} \iint_{A3} C_{ele\_lc} \\ C_{eqlc\_case3} &= \frac{3m^2 - 3m + 1}{3m^2} \iint_{A3} C_{ele\_lc} \end{aligned} \quad (20)$$

where  $C_{ele\_lc}$  is the elementary capacitance between the inner layer and core,  $A3$  is the boundary surface of the inner layer of the copper-foil inductor.

Based on the geometrical structure of the researched copper-foil inductor illustrated in Fig. 1 and the parameters are given in Table I, the equivalent permittivity  $\epsilon_{d3}$  between the inner layer and core of the researched copper-foil inductor,

which is dependent on the geometrical structure and material, is given as

$$\epsilon_{d3} = \frac{w_b \epsilon_b + (d_0 - w_b) p_1 + d_1 \epsilon_b + p_0}{w_b + d_0} \quad (21)$$

Then, the equivalent permittivity used for calculating the fringe field capacitance between the sidewall of winding and core, which is fully dependent on the geometrical structures and material information of designed inductors, is given in (22), approximately.

$$\epsilon_{d1\_new} \approx \frac{(p_1 + d_1 + p_0) \epsilon_{d3} + \frac{(1 + \epsilon_c)}{2} l_1}{l_1 + p_1 + d_1 + p_0} \quad (22)$$

The equivalent permittivity used for calculating the fringe field capacitance between the top-surface of winding and core is given in (23).

$$\begin{cases} \epsilon_{d2\_new} = \frac{(p_1 + d_1 + p_0) \epsilon_{d3} + \frac{(1 + \epsilon_c)}{2} t_{winding} + \pi l_2}{p_1 + d_1 + p_0 + t_{winding} + \pi l_2} & (l_2 < \frac{w_m - w_c}{2}) \\ \epsilon_{d2\_new} = 1 & (l_2 \geq \frac{w_m - w_c}{2}) \end{cases} \quad (23)$$

The equivalent capacitance between two adjacent layers is defined as (24). Due to the cylinder structure of the winding, the boundary surface of the inner layers is always less than the outer layers. Therefore, in order to simplify the model, the average boundary surface  $A4$  of all layers is used to be the surface integral.  $C_{ele\_ll}$  is the elementary capacitance between two adjacent layers.

$$C_{eqll} = \frac{(4m - 1)}{3m^2} \iint_{A4} C_{ele\_ll} \quad (24)$$

The equivalent capacitance between the two windings is quite dependent on the geometrical structure and winding layout. If the two windings are totally symmetrical, there is no parasitic capacitance. However, the geometrical structure illustrated in Fig. 1 is a quasi-symmetrical structure. Therefore, the equivalent capacitance between the two windings has to be considered. A schematic to illustrate the capacitive couplings between the two windings is given in Fig. 9. The voltage potential on the start point and endpoint of winding is assumed as  $V_1$  and  $(m-1)V_1/m$ , respectively.

The equivalent winding-to-winding capacitances in the Region I and II are presented as (25).  $A5\_1$  represents the boundary surface in 3-dimensional of Region I illustrated in Fig.8, where  $A5\_2$  represents the boundary surface in 3-dimensional of Region II.  $\epsilon_{d3}$  and  $\epsilon_{d4}$  are the equivalent permittivities in Region I and II, respectively.  $C_{eq\_ww}$  is the sum of the equivalent capacitance in Region I and II.

It is worth to mention that the elementary capacitances  $C_{ele\_lc}$ ,  $C_{ele\_ll}$ ,  $C_{ele\_ww}$  can be calculated according to [22].

The total capacitances for three cases are obtained by summing the equivalent capacitances in (19), (20), (24), and (25).

$$\left\{ \begin{array}{l} W_{ww_1} = \iint_{.A5_1} \frac{1}{2} \frac{\epsilon_{d3} \epsilon_0}{w_w + \sqrt{2}(l_3 + t_m)} \left[ \frac{bV_1}{4m(a+b)} + 0 \right]^2 dl_3 \\ \epsilon_{d3} = \frac{\sqrt{2}t_m \epsilon_m + \sqrt{2}l_3 + w_w}{\sqrt{2}t_m + \sqrt{2}l_3 + w_w} \\ C_{eq\_ww_1} = \frac{2W_{ww_1}}{(mV_1 - 0)^2} \\ W_{ww_2} = \iint_{.A5_2} \frac{1}{2} \frac{\epsilon_{d4} \epsilon_0}{w_w + 2t_m} \left[ \frac{bV_1}{4m(a+b)} + 0 \right]^2 dl_4 \\ \epsilon_{d4} = \frac{2\epsilon_m t_m + w_w}{2t_m + w_w} \\ C_{eq\_ww_2} = \frac{2W_{ww_2}}{(mV_1 - 0)^2} \\ C_{eq\_ww} = 2C_{eq\_ww_1} + C_{eq\_ww_2} \end{array} \right. \quad (25)$$

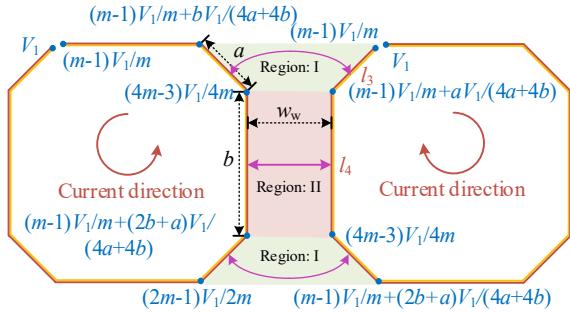


Fig. 9 Schematic of the capacitive coupling between two windings.

$$\left\{ \begin{array}{l} \text{Case 1: } C_{eqtotal1} = C_{eqfringe\_case1} + C_{eqle\_case1} + C_{eqll} + C_{eq\_ww} \\ \text{Case 2: } C_{eqtotal2} = C_{eqfringe\_case2} + C_{eqle\_case2} + C_{eqll} + C_{eq\_ww} \\ \text{Case 3: } C_{eqtotal3} = C_{eqfringe\_case3} + C_{eqle\_case3} + C_{eqll} + C_{eq\_ww} \end{array} \right. \quad (26)$$

A three-terminal equivalent circuit is illustrated in Fig. 10 for representing the copper-foil inductor.

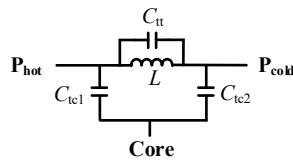


Fig. 10 Three-terminal equivalent circuit to represent the copper-foiled MV filter inductor

$P_{hot}$  is the terminal at the inner layer (hot layer),  $P_{cold}$  is the terminal at the outer layer (cold layer). The equivalent capacitance between the two terminals is  $C_{tt}$ , where the equivalent capacitance between the terminals and core are  $C_{tc1}$  and  $C_{tc2}$ , respectively.

Based on [22], the three equivalent capacitances in Fig. 10 are calculated by

$$\left\{ \begin{array}{l} C_{eqtotal1} = C_{tt} + \frac{C_{tc1} C_{tc2}}{C_{tc1} + C_{tc2}} \\ C_{eqtotal2} = C_{tt} + C_{tc2} \\ C_{eqtotal3} = C_{tt} + C_{tc1} \end{array} \right. \quad (27)$$

## V. MODEL VALIDATIONS

The parasitic capacitances of the copper-foil inductor introduced in Section II are analytically calculated by using the equations derived in Section IV.

A 10 kV/8 A copper-foiled inductor is manufactured based on the schematic given in Fig. 1, where the pictures are presented in Fig. 11.

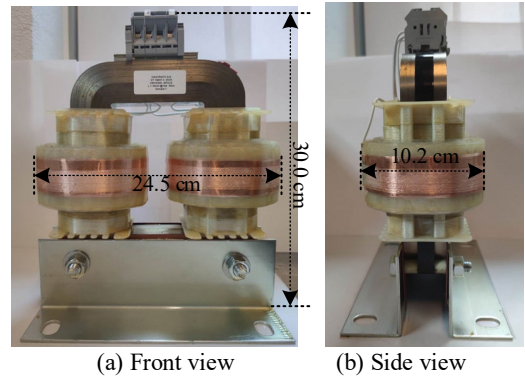


Fig. 11 Pictures of the manufactured copper-foiled MV filter inductor

### A. Theoretical calculation results

By using the derived equations (2)-(27) and physical parameters of the copper-foiled inductor, the calculated equivalent fringe field, inner layer to core, layer-to-layer, and winding-to-winding capacitances for the three different cases are listed in Table III. It is worth to mention that the calculated capacitances are only valid before the first resonant frequency of the copper-foiled inductor due to the assumptions used for calculating the elementary capacitance.

Based on (27), the three-terminal equivalent circuit of the researched inductor is presented in Fig. 12. The inductance value is used as the rated value of the researched inductor.

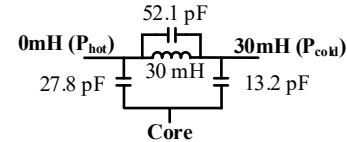


Fig. 12 Calculated three-terminal equivalent circuit of the researched copper-foiled MV inductor

### B. Experimental verifications

In this section, the parasitic capacitances of the copper-foiled inductor are measured to verify the theoretical analysis using a Keysight E4990A impedance analyzer [33] and its adapter 16047 [34], where the accuracy is between 0.1% and 1% for the measured impedance smaller than 100 kΩ. Before measuring the impedance of the inductors, both open-loop and short-circuit calibrations are applied to guarantee the

Table III Total capacitance for the three different cases

Case	Description	Equivalent fringe field capacitance	Equivalent layer to layer capacitance	Equivalent inner layer to core capacitance	Equivalent winding-to-winding capacitance	Total capacitance
Case1	Core is floating	6.1 pF	53.7 pF	1.3 pF	≈0 pF	61.1 pF
Case2	Core is connected to $P_{hot}$	11.6 pF		≈0 pF		65.3 pF
Case3	Core is connected to $P_{cold}$	4.8 pF		21.5 pF		80.0 pF

measurement accuracy. A picture of the experimental setup is given in Fig. 13.

The conventional measurement method and the guarding measurement method are used to measure the parasitic capacitance for the three different cases, where the core potential is different, as discussed in Section V. The principles of the two measurement methods are well described in [35]. The measured impedance is fitted by using an equivalent LC parallel circuit, which is integrated in Keysight E4990 impedance analyzer. Then, the inductance and capacitance of the equivalent LC parallel circuit are obtained.

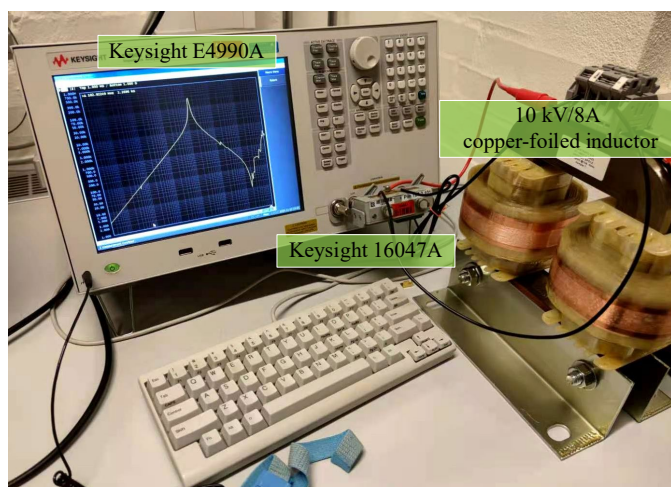


Fig. 13 Experimental setup for measuring the parasitic capacitances in an MV copper-foiled inductor

Fig. 14 shows the comparisons between the calculations and measurements. The dc-bias voltage and current are selected as 0 V and 0 mA in these three researched cases. More tests under different dc-bias voltage and current are measured, which is however, do not show any difference on the impedance around the first resonant point.

The value of inductance in the calculated impedance is derived with the known value of the designed (rated) inductance. Fig. 14(a)-(c) is the comparison between the theoretical calculations and measured impedance using the conventional measurement method. Fig. 14(d)-(f) is the comparison between the theoretical calculations and measured impedance when using guarding technology. Since there are no damping resistors in the calculated equivalent circuit, the magnitude at the resonance point in Fig. 14(a)-(d) is infinitely high. Therefore, the frequency of the first resonant points matches well, which means the calculations are close to the measured results. In Fig. 14(e) and (f), the calculated

impedance before the first resonant point (is smaller than 1MHz in this paper) is close to the measured impedance. The numerical comparisons are also given in Table. IV. Overall, the theoretical calculations show good agreement with the measurements.

### C. Comparisons

The modeling method introduced in [22] is used to calculate the parasitic capacitance of the same copper-foiled inductor, with the same geometrical and material parameters. The comparisons among the calculated three-terminal equivalent circuit using the method in [22], proposed method, and two different modeling methods are presented in Table IV.

For the three cases, compared to the measurements by using guarding technology, the calculated parasitic capacitance without considering the fringe field has 11.2%, 15.2%, and 13.5% error in three cases, respectively. The errors of calculations using the proposed method in the three cases are 1.0%, 3.2%, and 7.8%, respectively. The proposed modeling method has better accuracies with considering the fringe electrical field effects.

For the calculated three-terminal equivalent circuits, it can be found that the measured capacitance between  $P_{cold}$  and G is 11.0 pF by using the guarding technology, instead of the theoretical calculations 0 pF by using the modeling method in [22], which means the modeling method [22] fails to characterize the capacitance between the terminals and core. However, this capacitance is successfully characterized by using the proposed modeling method, where the fringe field effects is important in modeling the parasitic capacitances in copper-foiled inductors.

### D. Error analysis

The values of the geometrical and material parameters in the manufactured inductor cannot be the same as the designed value since the complex structure is utilized in the copper-foiled inductors. Several assumptions are made to simplify the electrical field distribution for analytically modeling the parasitic capacitance, which can introduce errors to the calculations. Besides, the measurements can also introduce errors. Especially the values can be easily changed by temperature, humidity, and so on. As can be seen from Table IV, the maximum difference between using two different measurement methods is close to 2%. However, in this article, the maximum error is observed as less than 10%, which is acceptable compared to relevant research [14], [22], [36], [37].

IEEE POWER ELECTRONICS REGULAR PAPER/LETTER/CORRESPONDENCE

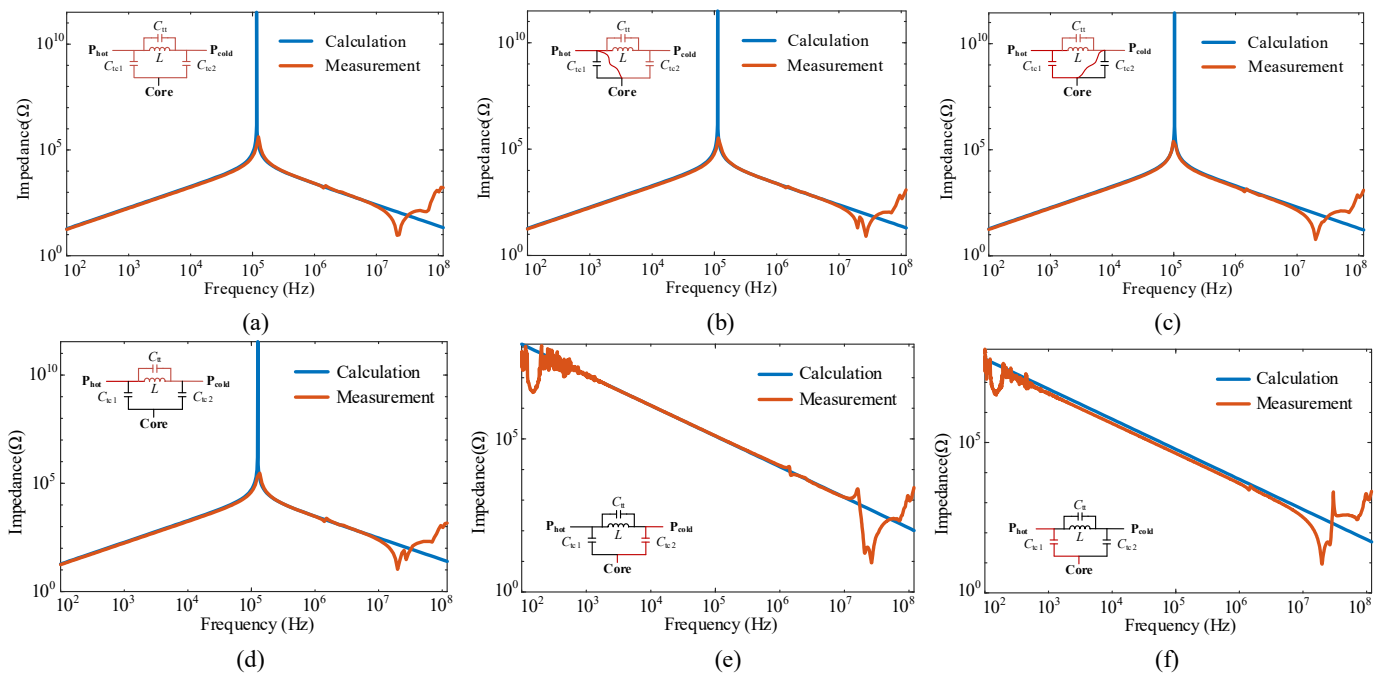


Fig. 14 Comparisons between the calculations and measured impedance (dc-bias voltage 0 V and current 0 A). (a)-(c) are Case 1, Case 2 and Case 3, respectively, by using the conventional measurement method; (d)-(f) are Case 1, Case 2 and Case 3, respectively, by using the measurement method with guarding technology.

Table IV Numerical comparisons of parasitic capacitances between the measurements and calculations

Case	Calculations (w/o considering the fringe field [22])	Calculations (Proposed method)	Measured capacitance (Normal measurements)	Converted capacitance based on the measurements with guarding method
Case 1	53.7 pF	61.1 pF	61.2 pF	60.5 pF
Case 2	53.7 pF	65.3 pF	65.3 pF	63.3 pF
Case 3	75.1 pF	80.0 pF	85.1 pF	86.8 pF
Two-terminal equivalent circuit				
Three-terminal equivalent circuit				

E. Recommendations for reducing the parasitic capacitances

Two recommendations for reducing the parasitic capacitances in copper-foiled inductors are obtained based on previous theoretical analysis:

- 1) The parasitic capacitance between two adjacent layers is able to be reduced with a larger number of layers used in the winding, according to (24).
- 2) The parasitic capacitance between the winding and core (fringe field capacitance and inner-layer-to-core capacitance) is able to be reduced by using spacers with a larger thickness, according to (15)-(18) and (20).

VI. CONCLUSIONS

The parasitic capacitances in copper-foiled MV filter inductor paper have been modeled in this article. Besides the conventional elementary capacitances, the elementary capacitances contributed by the fringe electrical field have been identified. A physics-based modeling method has been proposed to analytically calculate the parasitic capacitance contributed by the fringe electrical field, which is computationally efficient. A three-terminal equivalent circuit was further developed to characterize the couplings between the terminals and the core of the inductors. The measurements on a copper-foiled inductor have been presented. The experimental results verified the validity of the proposed modeling method, where the parasitic capacitance between the cold terminal and ground was failed to be revealed in the

IEEE POWER ELECTRONICS REGULAR PAPER/LETTER/CORRESPONDENCE

conventional modeling method without considering the fringe effects. Two recommendations for reducing the parasitic capacitance in copper-foiled inductors are also given in this paper.

REFERENCES

[1] J. Casady, V. Pala, D. Lichtenwalner, E. Brunt, B. Hull and et al., "New generation 10 kV SiC power MOSFET and diodes for Industrial Applications," in *Proc. Proceedings of PCIM Europe 2015*, May 2015, pp. 96-103.

[2] J. Wang, R. Burgos, D. Boroyevich and Z. Liu, "Design and testing of 1 kV H-bridge power electronics building block based on 1.7 kV SiC MOSFET module," in *Proc. 2018 International Power Electronics Conference*, May 2018, pp. 3749-3756.

[3] J. Casarin, P. Ladoux and P. Lasserre, "10kV SiC MOSFETs versus 6.5kV Si-IGBTs for medium frequency transformer application in railway traction," in *Proc. 2015 International Conference on Electrical Systems for Aircraft, Railway, Ship Propulsion and Road Vehicles*, Aachen, 2015, pp. 1-6.

[4] B. Zhang and S. Wang, "A Survey of EMI Research in Power Electronics Systems With Wide-Bandgap Semiconductor Devices," *IEEE Journal of Emerging and Selected Topics in Power Electronics*, vol. 8, no. 1, pp. 626-643, Mar. 2020.

[5] A. Anurag, S. Acharya and S. Bhattacharya, "Gate drivers for high-frequency application of silicon-carbide MOSFETs: design considerations for faster growth of LV and MV applications," *IEEE Power Electronics Magazine*, vol. 6, no. 3, pp. 18-31, Sep. 2019.

[6] X. Zhang, H. Li, J. Brothers, L. Fu, M. Perales, J. Wu and J. Wang, "A gate drive with power over fiber-based isolated power supply and comprehensive protection functions for 15-kV SiC MOSFET," *IEEE Journal of Emerging and Selected Topics in Power Electronics*, vol. 4, no. 3, pp. 946-955, Sep. 2016.

[7] N. Christensen, A. Jørgensen, D. Dalal, S. Sønderskov, S. Bęczkowski, C. Uhrenfeldt and S. Munk-Nielsen, "Common-mode current mitigation for medium voltage half-bridge SiC modules," in *Proc. 2017 19th European Conference on Power Electronics and Applications*, Sep. 2017, pp. 1-8.

[8] J. Jørgensen et al. "Multi-chip Medium Voltage SiC MOSFET Power Module with Focus on Low Parasitic Capacitance," in *Proc. 11th International Conference on Integrated Power Electronics Systems*, Mar. 2020, pp. 154-159.

[9] C. DiMarino, B. Mouawad, C. Johnson, M. Wang, Y. Tan, G. Lu, D. Boroyevich and R. Burgos, "Design and experimental validation of a wire-bond-less 10 kV SiC MOSFET power module," *IEEE Journal of Emerging and Selected Topics in Power Electronics*, Early access, doi: 10.1109/JESTPE.2019.2944138.

[10] Y. Xiao, Z. Zhang, M. Andersen, and K. Sun, "Impact on ZVS operation by splitting inductance to both sides of transformer for 1-MHz GaN based DAB converter," *IEEE Transactions on Power Electronics*, vol. 35, no. 11, pp. 11988-12002, Nov. 2014.

[11] Z. Ouyang and M. Andersen, "Overview of planar magnetic technology-fundamental properties," *IEEE Transactions on Power Electronics*, vol. 29, no. 9, pp. 4888-4900, Sep. 2014.

[12] J. Biela and J. Kolar, "Using transformer parasitics for resonant converters - a review of the calculation of the stray capacitance of transformers," *IEEE Transactions on Industry Applications*, vol. 44, no. 1, pp. 223-233, Jan./Feb. 2008.

[13] S. Acharya, A. Anurag, Y. Prabowo, and S. Bhattacharya, "Practical design considerations for MV LCL filter under high dv/dt conditions considering the effects of parasitic elements," in *Proc. 2018 9th IEEE International Symposium on Power Electronics for Distributed Generation Systems*, Jun. 2018, pp. 1-7.

[14] Z. Shen, H. Wang, Y. Shen, Z. Qin and F. Blaabjerg, "An improved stray capacitance model for inductors," *IEEE Transactions on Power Electronics*, vol. 34, no. 11, pp. 11153-11170, Nov. 2019.

[15] H. Zhao et al., "Behavioral modeling and analysis of ground current in medium-voltage inductors," *IEEE Transactions on Power Electronics*, vol. 36, no. 2, pp. 1236 - 1241, Feb. 2021.

[16] A. Anurag, S. Acharya, S. Bhattacharya and T. Weatherford, "Thermal performance and reliability analysis of a medium voltage three-phase inverter considering the influence of high dv/dt on parasitic filter elements," *IEEE Journal of Emerging and Selected Topics in Power Electronics*, vol. 8, no. 1, pp. 486-494, Mar. 2020.

[17] R. Ramachandran et al., "Analysis and Experimental Verification of Reducing Intra-winding Capacitance in a Copper Foil Transformer," in *Proc. 2020 IEEE Applied Power Electronics Conference and Exposition*, Mar. 2020, pp. 2653-2657.

[18] H. Kiwaki et al., "Evaluation of high power foil-type air-core transformer by high-frequency flyback converter," in *Proc. Proceedings of 1994 Power Electronics Specialist Conference*, Jun. 1994, pp. 1311-1314.

[19] E. Barrios et al., "High-Frequency Power Transformers With Foil Windings: Maximum Interleaving and Optimal Design," *IEEE Transactions on Power Electronics*, vol. 30, no. 10, pp. 5712-5722, Oct. 2015.

[20] R. Reeves et al., "Air-coiled foil-wound inductors," *Proceedings of the Institution of Electrical Engineers*, vol. 125, no. 5, pp. 460-464, May 1978.

[21] X. Liu et al., "Calculation of capacitance in high-frequency transformer windings," *IEEE Transactions on Magnetics*, vol. 52, no. 7, 2003204, Jul. 2016.

[22] H. Zhao et al., "Physics-based modeling of parasitic capacitance in medium-voltage filter inductors," *IEEE Transactions on Power Electronics*, vol. 36, no. 1, pp. 829 - 843, Jan. 2021.

[23] L. Deng et al., "Investigation on the Parasitic Capacitance of High Frequency and High Voltage Transformers of Multi-Section Windings," *IEEE Access*, vol. 8, pp. 14065-14073, Jan. 2020.

[24] N. Van der meijs and J. Fokkema, "VLSI circuit reconstruction from mask topology," *Integration*, vol. 2, no. 2, pp. 85-119, Jun. 1984.

[25] A. Massarani and M. K. Kazimierzczuk, "Self-capacitance of inductors," *IEEE Trans. Power Electron.*, vol. 12, no. 4, pp. 671-676, Jul. 1997.

[26] H. Wheeler, "Transmission-Line Properties of Parallel Strips Separated by a Dielectric Sheet," *IEEE Transactions on Microwave Theory and Techniques*, vol. 3, no. 2, pp. 172-185, Mar. 1965.

[27] A. Elrashidi et al., "Performance Analysis of a Microstrip Printed Antenna Conformed on Cylindrical Body at Resonance Frequency 4.6 GHz for TM01 Mode," *Procedia Computer Science*, vol. 10, pp. 775-784, 2012.

[28] Y. Wang et al., "The Fringe-Capacitance of Etching Holes for CMOS-MEMS," *Micromachines*, vol. 6, no. 11, pp. 1617-1628, Oct. 2015.

[29] Dupont Teijin Films, "Mylar polyester film," Jun. 2003. [Online]. Available: [http://usa.dupontteijinfilms.com/wp-content/uploads/2017/01/Mylar\\_Electrical\\_Properties.pdf](http://usa.dupontteijinfilms.com/wp-content/uploads/2017/01/Mylar_Electrical_Properties.pdf)

[30] LANXESS, "DURETHAN BKV 30 H-polyamide 6", May 2005. [Online]. Available: [https://techcenter.lanxess.com/scp/americas/en/docguard/PIB\\_Durethan\\_BKV30H.pdf?docId=76997](https://techcenter.lanxess.com/scp/americas/en/docguard/PIB_Durethan_BKV30H.pdf?docId=76997)

[31] Wikipedia, "Vacuum permittivity", Sep. 2019. [Online]. Available: [https://en.wikipedia.org/wiki/Vacuum\\_permittivity](https://en.wikipedia.org/wiki/Vacuum_permittivity)

[32] Metglas, "Magnetic materials" Aug. 2020. [Online]. Available: <https://metglas.com/magnetic-materials/>

[33] Keysight Technologies, "Keysight Technologies Impedance measurement handbook" [Online], Available: <https://literature.cdn.keysight.com/litweb/pdf/5950-3000.pdf>

[34] Keysight Technology, "E4990A Impedance Analyzer" [Online]. Available: <https://www.keysight.com/us/en/assets/7018-04256/data-sheets/5991-3890.pdf>

[35] Keysight Technology, "16047A Test Fixture" [Online]. Available: <https://www.keysight.com/en/pd-1000000477%3Aepeg%3Apro-16047A/test-fixture-axial-and-radial?pm=PI&nid=-34051.536880746&cc=DK&lc=dan>

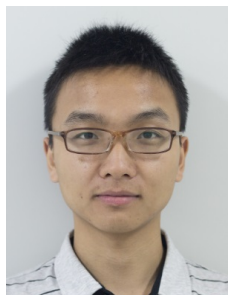
[36] P. Thummala, H. Schneider, Z. Zhang and M. Andersen, "Investigation of transformer winding architectures for high voltage (2.5 kV) capacitor charging and discharging applications," *IEEE Transactions on Power Electronics*, vol. 31, no. 8, pp. 5786-5796, Aug. 2016.

[37] M. Zdanowski, K. Kostov, J. Rabkowski, R. Barlik and H. Nee, "Design and Evaluation of Reduced Self-Capacitance Inductor in DC/DC Converters with Fast-Switching SiC Transistors," *IEEE Transactions on Power Electronics*, vol. 29, no. 5, pp. 2492-2499, May 2014.

IEEE POWER ELECTRONICS REGULAR PAPER/LETTER/CORRESPONDENCE



**Hongbo Zhao** received the B.S. degree in electrical engineering and its automation from Southwest Jiaotong University, Chengdu, China in 2015. He is currently working toward the Ph.D degree with Aalborg University, Aalborg, Denmark. His research interests include medium-voltage converters and their filters utilized by wide band-gap power devices.



**Zhizhao Huang** received the B.S. degree in new energy materials and devices from the University of Electronic Science and Technology of China, Chengdu, China, in 2015 and is currently working toward the Ph.D. degree in the School of Electrical and Electronic Engineering, Huazhong University of Science and Technology, Wuhan, China. From October 2019 to October 2020, He was a visiting Ph.D. student in the Power Electronic Systems Section at the Department of Energy Technology, Aalborg University, Aalborg, Denmark. His current research interests include wide bandgap devices packaging, integration, and high-density applications.



**Dipen Narendra Dalal** received the M.Sc. degree in Energy Engineering with specialization in Power Electronics and Drivers from Aalborg University, Aalborg, Denmark in 2016. He is currently working towards the PhD degree at the Department of Energy Technology, Aalborg University. His current research interests include wide band-gap power semiconductor devices and medium voltage high power converters.



**Asger Bjørn Jørgensen** received the M.Sc. and Ph.D. degrees in energy engineering from Aalborg University, Denmark, in 2016 and 2019, respectively. He is currently working as a Postdoc at the Department of Energy Technology, Aalborg University. His research interests include power module packaging, wide bandgap power semiconductor and multi-physics finite element analysis within power electronic applications.



**Jannick Kjær Jørgensen** received his M.Sc. degree in Nanotechnology with specialization in Nanomaterials and Nanophysics from Aalborg University, Aalborg, Denmark in 2018. He is currently working as a research assistant at the Department of Energy Technology, Aalborg university. His research interests include packaging and modeling of wide-bandgap power semiconductor devices, and medium voltage power modules.



**Xiongfei Wang** received the B.S. degree from Yanshan University, Qinhuangdao, China, in 2006, the M.S. degree from Harbin Institute of Technology, Harbin, China, in 2008, both in electrical engineering, and the Ph.D. degree in energy technology from Aalborg University, Aalborg, Denmark, in 2013. Since 2009, he has been with the Department of Energy Technology, Aalborg University, where he became an Assistant Professor in 2014, an Associate Professor in 2016, a Professor and Research Program Leader for Electronic Power Grid (eGrid) in 2018, and the Director of Aalborg University-Huawei Energy Innovation Center in 2020. He is also a Visiting Professor of power electronics systems with KTH Royal Institute of Technology, Stockholm, Sweden. His current research interests include modeling, dynamic analysis and control of power electronic converters and systems, power electronics for sustainable energy systems and electrical grids, high power converters and multi-converter systems. Dr. Wang serves as a Member-at-Large for Administrative Committee of IEEE Power Electronics Society (PELS) in 2020-2022, and as an Associate Editor for the IEEE TRANSACTIONS ON POWER ELECTRONICS, the IEEE TRANSACTIONS ON INDUSTRY APPLICATIONS, and the IEEE JOURNAL OF EMERGING AND SELECTED TOPICS IN POWER ELECTRONICS. He was selected into Aalborg University Strategic Talent Management Program in 2016. He has received six Prize Paper Awards in the IEEE Transactions and conferences, the 2016 Outstanding Reviewer Award of IEEE TRANSACTIONS ON POWER ELECTRONICS, the 2018 IEEE PELS Richard M. Bass Outstanding Young Power Electronics Engineer Award, the 2019 IEEE PELS Sustainable Energy Systems Technical Achievement Award, the 2020 IEEE Power & Energy Society Prize Paper Award, and Highly Cited Researcher in the Web of Science in 2019-2020.



**Stig Munk-Nielsen** received the M.Sc. and Ph.D. degrees from Aalborg University, Aalborg, Denmark, in 1991 and 1997, respectively. He is currently Professor at the Department of Energy Technology, Aalborg University. His research interests include LV and MV Si, SiC and GaN converters, packaging of power electronic devices, electrical monitoring apparatus for IGBTs, failure modes and device test systems. In the last ten years, he has been involved or has managed 10 research projects. Published 221 international power electronic papers being co-author or author.